Check for updates

Geophysical Research Letters

RESEARCH LETTER
10.1029/2021GL095032

Key Points:

- *S*-wave velocity structures beneath the Central Bransfield Basin (CBB) and adjacent areas are obtained by ambient noise tomography
- The back-arc extension is strongest in the northeastern CBB with associated mantle exhumation and gradually weakens toward the southwest
- The ridge–trench collision and subsequent detachment of the subducted Phoenix Plate initiated the back-arc extension of the CBB

Supporting Information:

Supporting Information may be found in the online version of this article.

Correspondence to:

W. Li and X. Yuan,
weili@gfz-potsdam.de;
yuan@gfz-potsdam.de

Citation:

Li, W., Yuan, X., Heit, B., Schmidt-Aursch, M. C., Almendros, J., Geissler, W. H., & Chen, Y. (2021). Back-arc extension of the Central Bransfield Basin induced by ridge–trench collision: Implications from ambient noise tomography and stress field inversion. *Geophysical Research Letters*, *48*, e2021GL095032. https://doi.org/10.1029/2021GL095032

Received 29 JUN 2021
Accepted 6 OCT 2021

Author Contributions:

Conceptualization: Wei Li, Xiaohui Yuan, Benjamin Heit, Javier Almendros
Data curation: Xiaohui Yuan, Benjamin Heit, Mechita C. Schmidt-Aursch, Javier Almendros
Funding acquisition: Xiaohui Yuan, Benjamin Heit, Mechita C. Schmidt-Aursch, Javier Almendros, Wolfram H. Geissler

© 2021 The Authors.
This is an open access article under the terms of the Creative Commons Attribution-NonCommercial License, which permits use, distribution and reproduction in any medium, provided the original work is properly cited and is not used for commercial purposes.

Back-Arc Extension of the Central Bransfield Basin Induced by Ridge–Trench Collision: Implications From Ambient Noise Tomography and Stress Field Inversion

Wei Li[1,2], Xiaohui Yuan[1], Benjamin Heit[1], Mechita C. Schmidt-Aursch[3], Javier Almendros[4], Wolfram H. Geissler[3], and Yun Chen[2,5]

[1]Deutsches GeoForschungsZentrum GFZ, Potsdam, Germany, [2]State Key Laboratory of Lithospheric Evolution, Institute of Geology and Geophysics, Chinese Academy of Sciences, Beijing, China, [3]Alfred-Wegener-Institut, Helmholtz-Zentrum für Polar- und Meeresforschung, Bremerhaven, Germany, [4]Andalusian Institute of Geophysics, University of Granada, Granada, Spain, [5]CAS Center for Excellence in Deep Earth Science, Guangzhou, China

Abstract The Bransfield Basin is a young (~4 Ma) back-arc basin related to the remnant subduction of the Phoenix Plate that once existed along the entire Pacific margin of the Antarctic Peninsula. Based on a recently deployed amphibious seismic network, we use ambient noise tomography to obtain the *S*-wave velocity structure in the Central Bransfield Basin (CBB). Combining with the stress field inverted from focal mechanisms, our images reveal that the CBB suffers a significant extension in the northwest-southeast direction. The extension is strongest in the northeastern CBB with associated mantle exhumation and weakens to the southwest with decoupled deformations between the upper crust and lithospheric mantle. Such an along-strike variation of extension can be explained by slab window formation and forearc rotation, which are associated with the Phoenix Plate detachment during the ridge–trench collisions at the southwest of the Hero Fracture Zone.

Plain Language Summary Crustal extensions behind volcanic arcs are commonly attributed to subduction processes, however, subduction alone is not sufficient to trigger the back-arc extension as the latter is missing in some ongoing subduction zones. An effective way to assess the sufficient condition is to learn how the back-arc extension initiates. Here, we examine the recently formed Central Bransfield Basin (CBB), located off the Antarctic Peninsula in the back-arc setting of the Phoenix subduction zone. The stress field inverted from focal mechanisms indicates a northwest-southeast extension in the CBB. *S*-wave velocity structures imaged by ambient noise tomography show that the extension has distinctly different degrees along the axis of the CBB, which is strongest with associated mantle exhumation in the northeast and gradually weakens toward the southwest. Our observations suggest that the back-arc extension of the CBB, which started at ~4 Ma, was initiated by the ridge–trench collision at the southwest of the Hero Fracture Zone. With the subduction zone progressively eliminated during the ridge–trench collisions, the subducted Phoenix Plate has detached along the segmental Phoenix-Antarctic Ridge to form the slab window and trigger the forearc rotation, that initiated the back-arc extension of the CBB.

1. Introduction

Back-arc basins, characterized by intense extension behind island arcs or along continental margins adjacent to trenches, are commonly attributed to subduction processes involving multiple thermal and mechanical factors (Molnar & Atwater, 1978; Sdrolias & Müller, 2006; Stern, 2002). However, it remains a matter of debate if subduction alone is sufficient for initiating the back-arc extension (Mantovani et al., 2001; McCabe, 1984; Uyeda & Kanamori, 1979; Wallace et al., 2005), because back-arc basins are missing in some subduction zones, or extension has ceased while subduction is still active.

The Bransfield Basin separates the inactive island arc (i.e., South Shetland Block, SSB) from the northern tip of the Antarctic Peninsula (AP), beneath which the Phoenix Plate is subducting (Figure 1). The Phoenix Plate was formed by seafloor spreading since the Mesozoic at the Pacific-Phoenix and Farallon-Phoenix Ridges, and later on (~60 Ma) at the Antarctic-Phoenix Ridge (Eagles et al., 2004; Eagles & Scott, 2014). The subduction of the Phoenix Plate had led the Antarctic-Phoenix Ridge to successively converge with the AP from southwest to northeast since ~50 Ma (Eagles & Jokat, 2014; Larter & Barker, 1991). The present

Investigation: Xiaohui Yuan, Benjamin Heit, Mechita C. Schmidt-Aursch, Javier Almendros, Wolfram H. Geissler
Methodology: Wei Li, Mechita C. Schmidt-Aursch, Wolfram H. Geissler, Yun Chen
Project Administration: Javier Almendros
Supervision: Xiaohui Yuan, Yun Chen
Writing – original draft: Wei Li, Xiaohui Yuan
Writing – review & editing: Wei Li, Xiaohui Yuan, Benjamin Heit, Mechita C. Schmidt-Aursch, Javier Almendros, Wolfram H. Geissler, Yun Chen

trench, that once extended along the entire Pacific margin of the AP throughout the Mesozoic (Birkenmajer, 1994; Leat & Riley, 2021), is the remnant subduction site that was progressively eliminated from southwest to northeast during a series of ridge–trench collisions (Eagles & Jokat, 2014; Larter & Barker, 1991; Livermore et al., 2000). The Bransfield Basin has suffered extension since ∼4 Ma (Larter & Barker, 1991; Smellie, 2021), synchronously with the latest ridge–trench collision at the southwest of the Hero Fracture Zone (Larter & Barker, 1991; Lodolo & Pérez, 2015). As a young back-arc basin formed in a long-term subduction setting, the Bransfield Basin is an ideal site to learn how the back-arc extension initiates and what is the driving mechanism behind its evolution.

The opening of the Bransfield Basin has been accompanied by extensive volcanism aligned in the northeast-southwest direction and perpendicular to the extension direction (Figure 1b). Particularly in the Central Bransfield Basin (CBB), bounded by morphological steps at the large Quaternary volcanic islands, that is, Deception Island (DI) and Bridgeman Island (BI; Smellie, 2002, 2021), a series of submarine volcanic edifices stick out of the basin floor (Gràcia et al., 1996) with hydrothermal activity (Klinkhammer et al., 2001; Petersen et al., 2004; Rodrigo et al., 2018) and moderate-to-intense seismicity (Almendros et al., 1997, 2018; Dziak et al., 2010; Jiménez Morales et al., 2017; Robertson Maurice et al., 2003). The bathymetry in the CBB is markedly asymmetric with a narrow and steep margin adjacent to the SSB, in contrast, its southeastern margin adjacent to the AP consists of a flat shelf dissected by north- to northwest-trending troughs (Figure 1b; García et al., 2009). Controlled by the geomorphic features and glacial processes, the depocenter with ∼2-km-thick sedimentary extends from the southeast of volcanic edifices to the troughs in the AP shelf (Barker & Austin, 1998; Christeson et al., 2003; García et al., 2008; Prieto et al., 1998). Given that shallow igneous materials were geophysically observed in the rift centers (Almendros et al., 2020; Catalán et al., 2013; Christeson et al., 2003; Galindo-Zaldívar et al., 2004; Janik et al., 2014) and erupted lavas resemble mid-ocean ridge basalt (MORB; Fretzdorff et al., 2004; Haase & Beier, 2021), the CBB might be in an incipient stage of seafloor spreading (Catalán et al., 2013; Gràcia et al., 1996). Previous wide-angle seismic observations depict variations in the crustal thickness in the CBB reaching a minimum of 8–10 km in the northeast and generally thickening to ∼15 km in the southwest (Barker et al., 2003; Christeson et al., 2003). Considering current shear motion in the Eastern Bransfield Basin (EBB; González-Casado et al., 2000; Gràcia et al., 1996) and GPS measurements around the Bransfield area (Berrocoso et al., 2016; Taylor et al., 2008), rifting in the CBB has been proposed to propagate from northeast to southwest (Barker & Austin, 1998; Lodolo & Pérez, 2015; Vuan et al., 2005).

To investigate the submarine volcanoes and rift dynamics along the Bransfield Basin, comprehensive geophysical experiments have been conducted in the CBB between 2017 and 2020 within the BRAnsfield VOlcanoes SEISmology (BRAVOSEIS) project (Almendros et al., 2020). The deployment of a dense, amphibious broadband seismic network (Figure 1b) offers an excellent opportunity to image high-resolution crustal structures in the CBB and adjacent areas. Here, based on these new seismic observations, we perform ambient noise tomography to image *S*-wave velocity (Vs) structures in this area. The ambient noise interferometry can obtain interstation surface wave signals with dominant energy at relatively shorter periods (Bensen et al., 2007; Shapiro et al., 2005) and provide a holistic perspective of the crust beneath the CBB, which will help to yield new insights on the initiation mechanism of back-arc extension when integrating with the stress field and regional tectonics.

2. Data and Methods

The data used in this study are mainly from the amphibious broadband seismic network deployed within the BRAVOSEIS project (Figures 1b and Figure S1 in Supporting Information S1), which includes fourteen onshore stations (network 5M; Heit et al., 2020) and eight ocean-bottom seismometer (OBS) stations (network ZX; Schmidt-Aursch et al., 2021). They were deployed across the CBB, the SSB, and the AP shelf between 2018 and 2020 with an average interstation distance of ∼30 km. We also collect data from two synchronously running permanent seismic stations operated by the Istituto Nazionale Di Oceanografia E Di Geofisica Sperimentale (1992) (network AI). Additionally, six seismic stations (network XB) that operated between 1997 and 1999 (Wiens, 1997) are also analyzed. Continuous waveforms of the vertical component from 30 broadband seismic stations are collected to calculate cross-correlations for all available station pairs similar to previous studies (Bensen et al., 2007; Ritzwoller & Feng, 2019; Figure S2 and Data Set S1 in

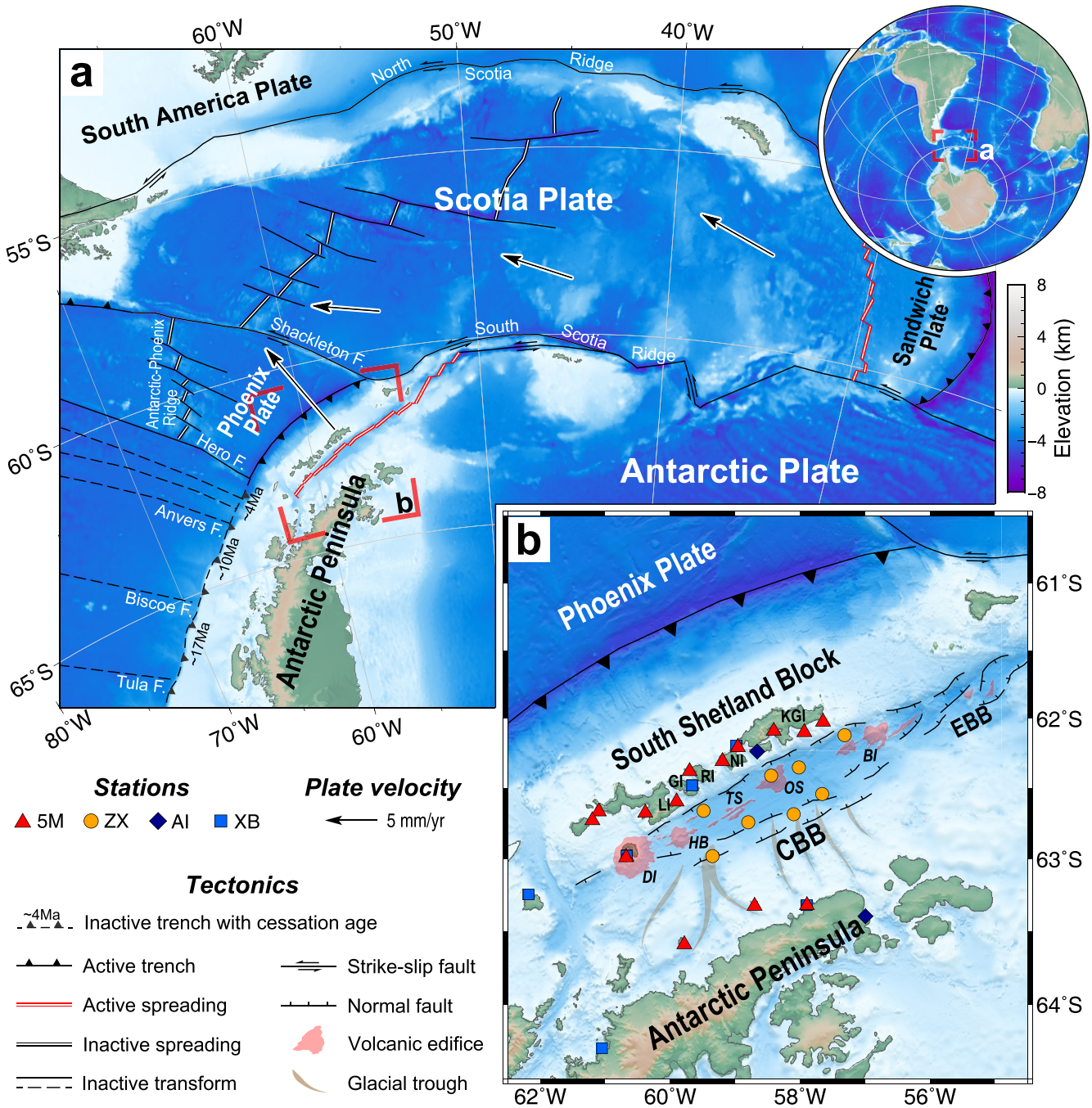

Figure 1. (a) Tectonic setting in and around the northern tip of the Antarctic Peninsula, which location is marked in the globe inset. The absolute plate motions fixed to the Antarctic Plate from the NNR-MORVEL56 (Argus et al., 2011) are plotted as black arrows. Red box represents the region of the Bransfield Basin and the South Shetland Block (SSB) in (b). (b) Topographic and tectonic map of the Bransfield Basin and the SSB. The Central (CBB) and Eastern (EBB) Bransfield Basin are characterized by linearly distributed volcanic edifices shown as translucent red areas, including Deception Island (DI), Humpback Seamount (HB), Three Sisters Ridge (TS), Orca Seamount (OS), and Bridgeman Island (BI) in the CBB. The SSB consists of several islands, including Livingston Island (LI), Greenwich Island (GI), Robert Island (RI), Nelson Island (NI), and King George Island (KGI). Stations (networks 5M, ZX, AI, and XB) used in this study are marked as symbols indicated in the legend.

Supporting Information S1). We manually extract Rayleigh wave group and phase velocity dispersions from cross-correlations using the Computer Programs in Seismology (CPS) package (Herrmann, 2013; Figure S3 in Supporting Information S1). Finally, we obtain nearly 250 group and phase velocity dispersion curves in the periods of 1–24 s (Figure S4 in Supporting Information S1), which cover well the study region (Figure

S5 in Supporting Information S1). Supporting Information S1 includes more details of these processes (Text S1 and Figures S2–S5 in Supporting Information S1). In this study, we apply the direct inversion method of surface wave dispersion proposed by Fang et al. (2015) to construct a three-dimensional (3-D) Vs model (Data Set S2 in Supporting Information S1) without the intermediate step of inverting phase or group velocity maps. Supporting information S1 provides more details of the direct inversion method and reliability tests (Text S2 and S3 and Figures S6–S9 in Supporting Information S1). We also use the MSATSI package (Martínez-Garzón et al., 2014) to invert the present-day stress field of the northeastern CBB from focal mechanisms (see details in Text S4 in Supporting Information S1), that help to further understand the geodynamic evolution of the crust and uppermost mantle structure imaged in the 3-D Vs model.

3. Results

Based on the data coverage and the resolution tests (Figures S5, S6, S8, and S9 in Supporting Information S1), we mainly focus on the 3-D Vs model between 0 and 35 km depth in the CBB and adjacent areas (Figures 2 and 3). At depths shallower than 5 km, the CBB shows two prominent low-Vs anomalies (<2.8 km/s) at the east of the Orca Seamount (OS) and between the Humpback Seamount (HB) and the Three Sisters Ridge (TS; Figures 2a, 2b and 3). These low-Vs anomalies show clear zonation along glacial troughs extending from the AP shelf (Figures 2a and 2b; García et al., 2009), with a large sedimentary thickness depicted by seismic reflection (García et al., 2008). The lowest Vs (<2.0 km/s at 1-km depth) appearing east of the OS is coincident with the depocenter covered by the thickest sedimentary layer (~2.6 km thick) in the CBB (Barker & Austin, 1998; Christeson et al., 2003; Prieto et al., 1998). The Vs model also contains relatively low-Vs anomalies (~3.4 km/s) at 10–15-km depth beneath the DI and 15–25-km depth beneath the Livingston Island (LI; Figures 2c, 2d and 3). Previous local seismic tomography (Zandomeneghi et al., 2009) and magnetotelluric study (Pedrera et al., 2012) image shallow magmatic or hydrothermal activity as low-Vs and high-conductivity anomalies beneath the DI and the LI. The relatively low-Vs anomalies imaged in this study possibly depict the deeper plumbing system there (Geyer et al., 2019), although their scale cannot be ensured due to the resolution of Vs model (Figure S8 in Supporting Information S1).

The most prominent feature in the 3-D Vs model is the contrasting crustal structures beneath the CBB and the SSB (Figures 2 and 3). The varying sedimentary thicknesses lead to low Vs (<2.8 km/s at 5-km depth) beneath the CBB but high Vs (>3.2 km/s at 5-km depth) beneath the SSB in the shallow as aforementioned, but the patterns are entirely different at depths deeper than ~15 km, which show significantly high Vs (>4.1 km/s) referring to the mantle beneath the CBB but low Vs (3.7–3.9 km/s) still referring to the crust beneath the SSB. These contrasting features reflect different crustal thickness beneath the CBB and the SSB. As shown in the cross sections (Figure 3), Moho depths indicated by previous H–κ stacking results (Biryol et al., 2018; Parera-Portell et al., 2021) are mostly close to the depth of the 4.0-km/s contours of the Vs model, that is, both are ~30-km depth beneath the SSB and the AP. We therefore use the depth of the 4.0-km/s contours as approximate Moho depths (Figure S10 in Supporting Information S1), which shows that the crust in the CBB is thinnest (~10 km) near the OS and thickens to ~20-km beneath the DI along the rift center. The crustal thickness is asymmetric across the CBB, like the bathymetry, that is an abrupt change in a narrow margin to the SSB but a gentle thickening in a relatively wide margin to the AP (Figure 3). The trend of the approximate Moho depths is mostly consistent with receiver function H–κ stacking results beneath the SSB and the AP (Biryol et al., 2018; Parera-Portell et al., 2021), and with the crustal thicknesses in the CBB revealed by wide-angle seismic surveys (Barker et al., 2003; Christeson et al., 2003). Seismic observations show that the P-wave velocity (Vp) will jump from 6.0–6.3 km/s in the upper crust to 6.6–6.8 km/s in the lower crust at the Conrad discontinuity (Christensen & Mooney, 1995; Wever, 1989). Thus, we refer to the 3.7-km/s contours of the Vs model (Vp ≈ 6.4 km/s, assuming a Vp/Vs ratio of 1.73) as the approximate interface between the upper and the lower crust here. The 3.7-km/s contours are almost constantly at 10-km depth with slight fluctuations in the study area (Figure 3), which indicates that the strong crustal thickness variation mainly reflects the significant thinning of the ductile lower crust beneath the CBB. The thickness of the lower crust is ~10 km beneath the DI, half as much as that beneath the SSB (~20 km) and is too thin to be identified beneath the OS (Figure 3). Although the surface wave method cannot accurately determine the discontinuity depth, synthetic tests indicate that our result can well image the trends of these discontinuities (Figure S11 in Supporting Information S1).

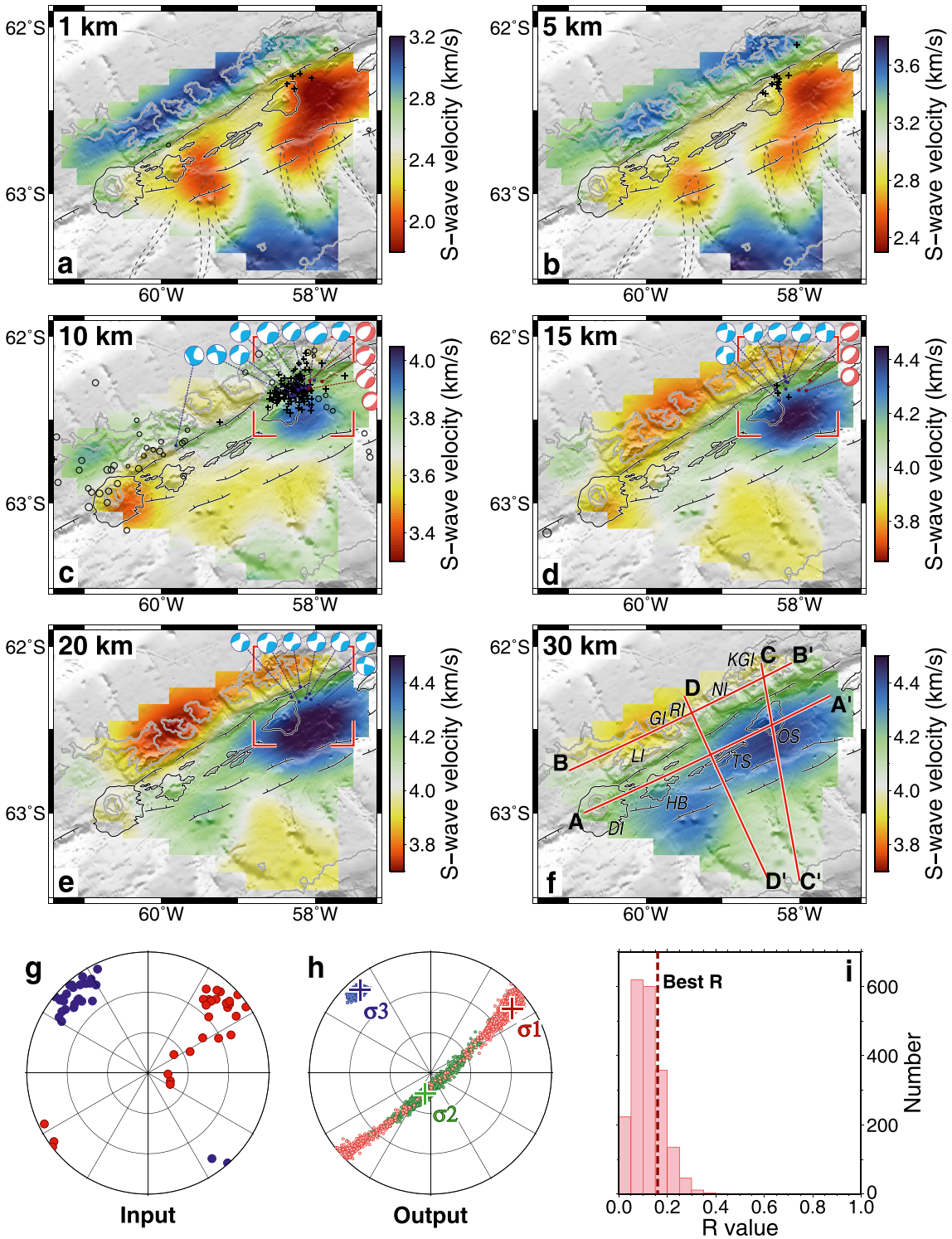
1 km
5 km
10 km
15 km
20 km
30 km
62°S
63°S
60°W
58°W
S−wave velocity (km/s)
KGI
NI
GI
RI
LI
TS
OS
HB
DI
A
A'
B
B'
C
C'
D
D'
Input
Output
σ1
σ2
σ3
Best R
R value
Number

Figure 2.

4. Discussion

4.1. Variations of Extensional Stage in the Central Bransfield Basin

The crustal structures observed in the 3-D Vs model exhibit features that are key to understanding the deformation and evolution of the Bransfield Basin. Foremost, the thinnest crust (~10 km) and the thickest sedimentary layer (~2 km) in the northeastern CBB indicate an intense crustal thinning that mainly affected the lower crust (Figures 2 and 3). Interestingly, there was a sharp increase of seismic activity in August 2020 in the northeast vicinity of the OS, where an abrupt change exists between the thickest crust beneath the SSB and thinnest crust beneath the basin (Figures 2 and 3). According to the earthquake location information from the USGS and the focal mechanisms from the gCMT, these earthquakes extend from the crystalline basement beneath the sedimentary basin to the Moho, and some of them are possibly located in the uppermost mantle (Figure 3). The present-day stress field of the northeastern CBB has a northwestward, horizontal minimum stress ($\sigma 3$) and a small stress ratio (R; Figure 2), which indicate that the stress field in this area is mainly organized by the northwest-southeast extension. The deep-seated seismic activities with extensional mechanism hint at coupled deformations throughout the crust and mantle lithosphere after the extreme necking of the ductile lower crust (Figure 4a). This is suggesting a hyperextension phase with possible mantle exhumation at the final transition stage from the continental rift to the seafloor spreading (Pérez-Gussinyé, 2013; Peron-Pinvidic et al., 2013). Furthermore, the predominant MORB-like lavas in the OS, sourced from the high-degree partial melting of the enriched mantle at relatively shallow depths (Fretzdorff et al., 2004; Haase & Beier, 2021; Keller et al., 2002), also support the strong lithospheric extension and possible mantle exhumation there.

In the southwestern CBB, the basin floor becomes progressively shallower through a series of morphological steps (Barker & Austin, 1998; Gràcia et al., 1996), and the crust gradually thickens to ~20-km thickness beneath the DI mainly due to the lower crustal thickening (Figure 3). In this area, seismic activity mainly limits to some shallow seismic swarms induced by the magmatic and hydrothermal activity (Almendros et al., 2018; Jiménez Morales et al., 2017). The significantly reduced seismicity in the deep crust (Figures 2 and 3) implies decoupled deformations between the upper crust and the lithospheric mantle, accommodated by the less-necked lower crust (Figure 4a). The generally increasing $(Ce/Yb)_N$ and Nb/Yb in the incompatible element ratios of the lavas toward the DI also reflect decreasing partial melting degrees of mantle sources (Haase & Beier, 2021). Therefore, the southwestern CBB is currently experiencing a thinning phase, it should be at a less-extending stage compared to the hyperextension phase that is occurring in the northeast (Pérez-Gussinyé, 2013; Peron-Pinvidic et al., 2013).

4.2. Initiation Mechanism of the Central Bransfield Basin Extension

Our images reveal that the CBB displays significant extension with possible mantle exhumation associated in the northeast (Figures 2, 3 and 4a). As the Bransfield Basin is situated in a back-arc setting, the rollback of the subducted Phoenix Plate has been proposed as the favored model for the initiation of the extension in the Bransfield Basin (Figure 4b; e.g., Dziak et al., 2010; Galindo-Zaldívar et al., 2004; Larter & Barker, 1991). The subducted Phoenix Plate, suggested to be located beneath the Bransfield Basin, is also supported by the high concentrations of fluid-mobile elements in the lavas (Fretzdorff et al., 2004; Haase & Beier, 2021) and can be seen in the seismic tomographic images as the southeastward dipping high-velocity anomaly extending from the trench to ~300-km depth (Lloyd et al., 2020; Park et al., 2012; Figure 4c and Figure S12 in Supporting Information S1). Plate reconstruction revealed that the western segments of the Antarctic-Phoenix Ridge have collided with the trench step by step and have subducted below it (Eagles & Jokat, 2014; Larter &

Figure 2. (a–f) Horizontal slices of the Vs model at depths of 1, 5, 10, 15, 20, and 30 km, respectively. Earthquakes within ±2.5-km swath along each slice are plotted as circles for the Reviewed ISC Bulletin (1964–2018; https://doi.org/10.31905/D808B830) and crosses for the recent USGS Catalog (2019–2020; http://earthquake.usgs.gov). Beach balls denote focal mechanisms (1976–2020) within the same swath downloaded from the gCMT (http://globalcmt.org). The compressional quadrants of focal mechanisms are colored as blue for strike-slip faulting and red for normal faulting. Red boxes indicate the region, where focal mechanisms are used for the stress field inversion. Red lines delineate the locations of the cross sections displayed in Figure 3. Volcanic edifices in the CBB are delineated with black lines, and coastlines are shown as gray lines. Dashed lines represent glacial troughs extending from the Antarctic Peninsula shelf. Abbreviations are the same as in Figure 1b. (g) Compression (red) and tension (blue) axes of focal mechanisms used as the input of the stress field inversion are shown in the stereo net. (h) Result of the stress field inversion. Crosses represent inverted principal stress axes. Colored points represent the 95% confidence level of the results estimated in bootstrap inversions. (i) Distributions of stress ratio ($R = (\sigma 1 - \sigma 2)/(\sigma 1 - \sigma 3)$).

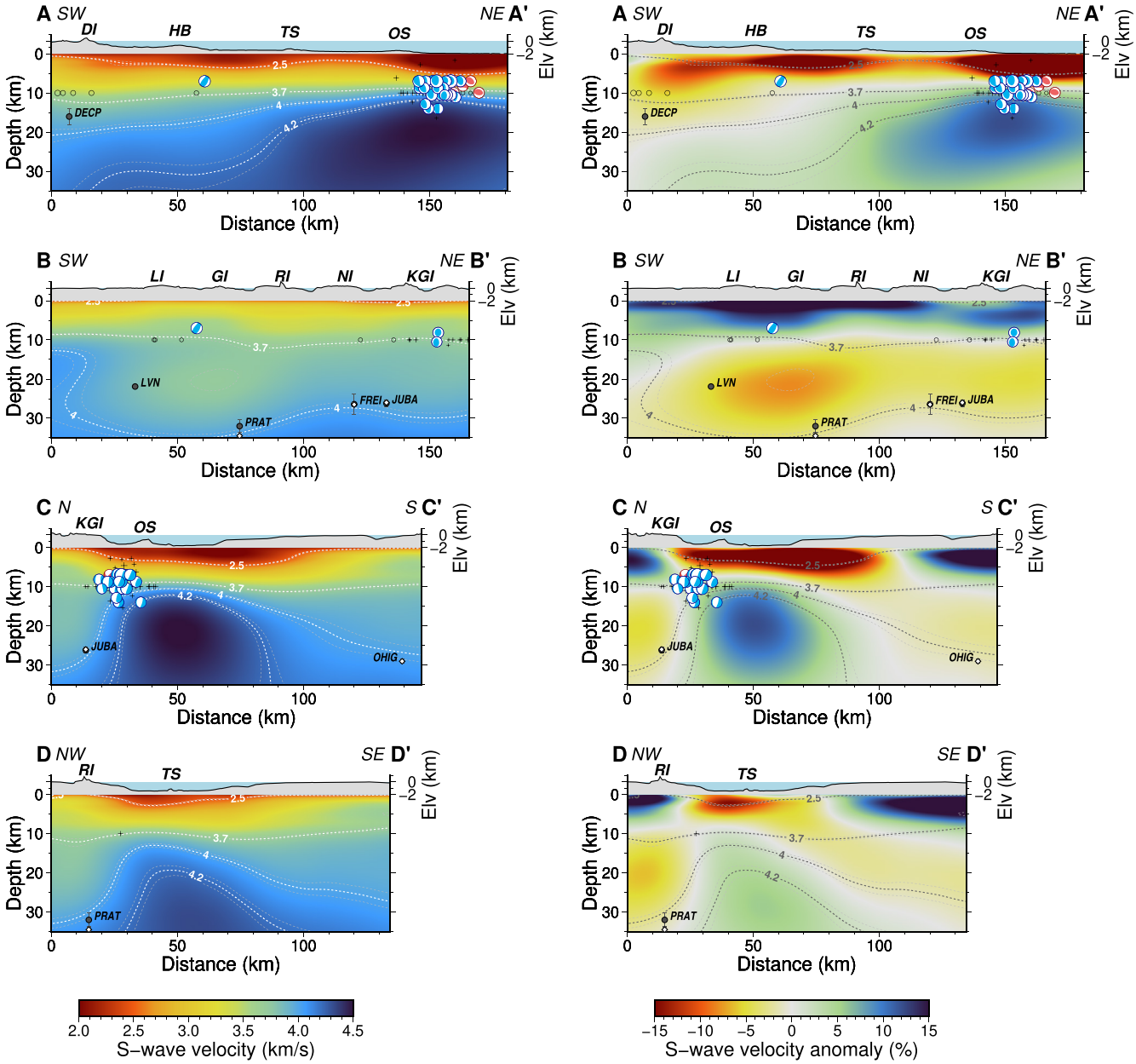

Figure 3. Vertical cross sections of the Vs model and corresponding Vs perturbation along lines AA, BB, CC, and DD indicated in Figure 2f. Vs perturbations are relative to the average value at each depth of the Vs model. Topography is plotted above each cross section with labels representing the locations of volcanic edifices and islands, abbreviations are the same as in Figure 1b. Earthquakes along each cross section with ±10-km swath are denoted as circles and crosses for different catalogs same as Figure 2. Similarly, focal mechanisms from the gCMT in the same swath are also projected onto each section and displayed using the half-sphere behind the plane. The points with error bars represent the Moho depth from previous H–κ stacking results (white ones from Biryol et al. [2018] and black ones from Parera-Portell et al. [2021]). White and black dashed lines show the contour lines of certain Vs with the ±0.025-km/s range bounded by the dashed lines.

Barker, 1991). With the subduction zone progressively eliminated during the ridge–trench collisions along the AP, the western part of the Phoenix Plate has been detached and a slab window has opened while the subduction continues in the eastern part (Figure 4b; Barker & Austin, 1998; Burkett & Billen, 2010). Such a slab window is well depicted by the adjoint tomography (Lloyd et al., 2020; Wiens et al., 2021) as a low-velocity gap between the slab-related high-velocity anomalies emerging at >150-km depth and the ceased trench at the southwest of the Hero Fracture Zone (Figure 4c and Figure S12 in Supporting Information S1). Consequently, it became progressively easier for mantle material to flow around the slab and slab rollback

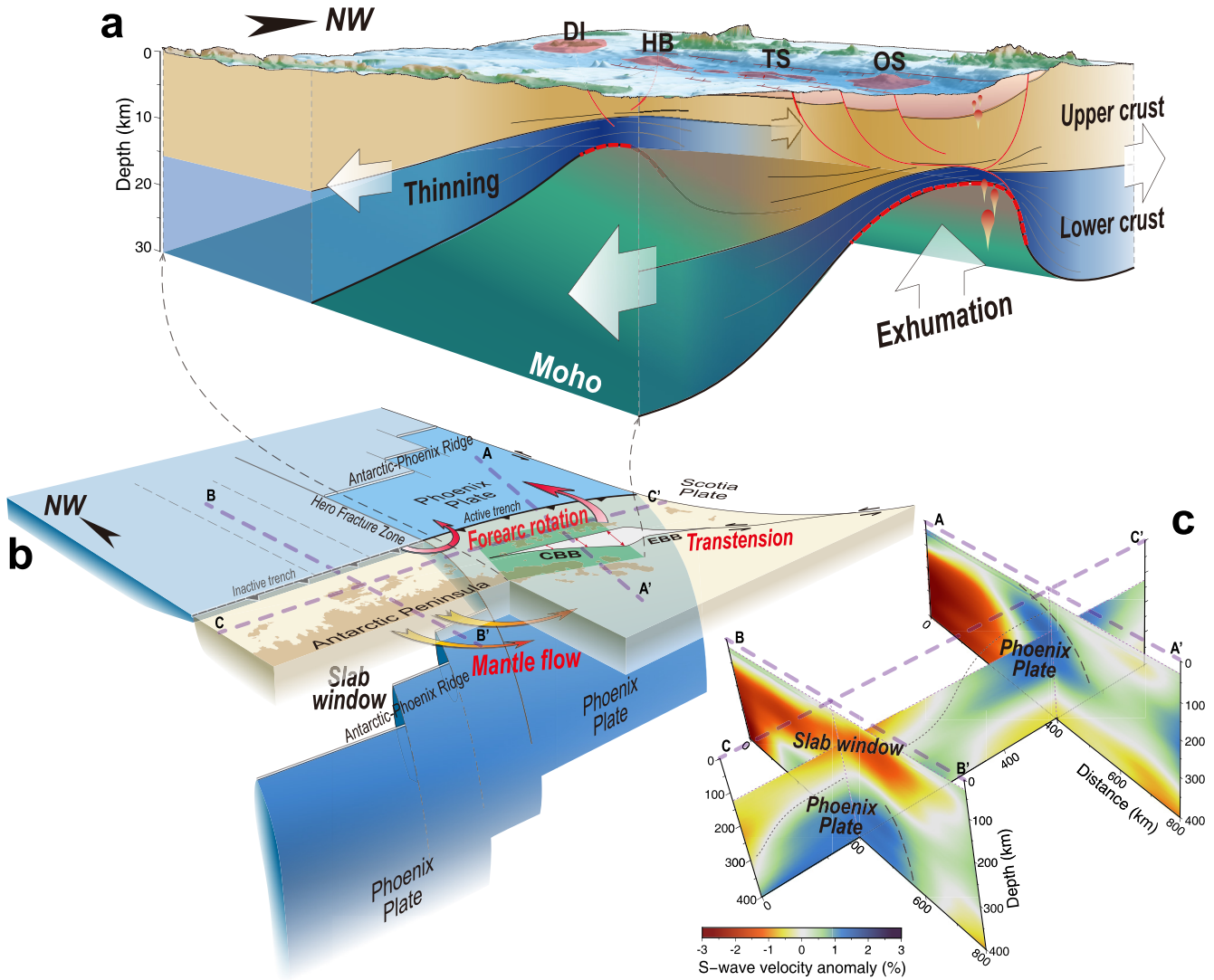

Figure 4. (a) Cartoon of the discrepant extensions in the CBB. The crust in the CBB is remarkably thin induced by northwest-southeast extension and mainly depicts ductile lower crustal necking. The lower crust is so thinned that faults can deeply penetrate through the crust in the northeast. Whereas the less-thinned lower crust in the southwest decouples upper crust and lithospheric mantle deformations. (b) Cartoon of the ridge–trench collision accounting for the initiation of back-arc extension in the CBB. Slab rollback is promoted by the mantle flow through the slab window formed by the detachment of the subducted Phoenix Plate. The collision of the remaining buoyant plate and the Antarctic Peninsula caused the forearc rotation, causing along-strike variation of the extension in the CBB. The transtension related to the shear motion between the Scotia Plate and the Antarctic Plate might further contribute to this extensional regime. (c) 3-D view of three cross sections extracted from the upper mantle Vs model imaged by the previous adjoint tomography (details are shown in Figure S12 in Supporting Information S1, original model is from Lloyd et al., 2020). These cross sections are plotted as Vs perturbation along purple lines AA, BB, and CC indicated in (b), and well depict the subducted Phoenix Plate and the slab window interpreted in (b).

started to initiate back-arc extension (Figure 4b). This ridge–trench collision model with the subsequent detachment of the subducted Phoenix Plate can explain why the back-arc extension has only developed in the Bransfield Basin, but not along the entire margin of the AP which was also affected by the subduction of the Phoenix Plate (Eagles & Jokat, 2014; Larter & Barker, 1991).

The Vs model also suggests that the crust extension gradually weakens from northeast to southwest in the CBB. The crust is thicker (~20-km thickness) in the southwestern CBB with decoupled deformations between the upper crust and the lithospheric mantle (Figures 3 and 4a). Such an along-strike variation of the back-arc extension can be excepted by the partial collision in the subduction system, which can generate forearc rotation around a nearby pole and lead to the strongest back-arc extension at the far end (Moresi et al., 2014; Wallace et al., 2005, 2009). After the Phoenix Plate detached along the Antarctic-Phoenix Ridge

(Larter & Barker, 1991), the remaining buoyant plate separated from the Phoenix Plate by the ridge had collided with the margin of the AP (Eagles & Jokat, 2014; Figure 4b). Therefore, we propose that the latest collision of the remaining buoyant plate and the AP at the southwest of the Hero Fracture Zone caused the forearc rotation of the SSB, which should have resulted in the strongest extension in the northeastern part of the CBB but weakest in the southwest (Figures 4a and 4b). Moreover, left-lateral shear motion between the Scotia Plate and the Antarctic Plate might cause transtension in the EBB (González-Casado et al., 2000; Gràcia et al., 1996) and contribute to the further development of the extensional regime in the CBB (Barker & Austin, 1998; González-Casado et al., 2000; Lodolo & Pérez, 2015).

5. Conclusions

We construct a 3-D Vs model of the CBB and adjacent areas by ambient noise tomography and invert the present-day stress field from focal mechanisms. Our new model reveals coupled deformations throughout the lithosphere in the northeastern CBB and decoupled deformations between the upper crust and lithospheric mantle in the southwest, indicating that along its strike, the CBB is suffering different extensional phases of continental rift-seafloor spreading transition. We suggest that the along-strike variation of extension was a consequence of the slab window formation and the forearc rotation, which are associated with the Phoenix Plate detachment during the ridge–trench collision at the southwest of the Hero Fracture Zone. The role of the Phoenix Plate in this process implies that the ridge–trench collision and subsequent slab detachment are the main initiation mechanism of back-arc extension in the CBB.

Data Availability Statement

Continuous data of the onshore stations of the BRAVOSEIS project are archived at the GEOFON Data Centre (5M, Heit et al., 2020). The OBS data are archived at the PANGAEA repository (ZX, Schmidt-Aursch et al., 2021). The data from permanent stations and other temporary stations can be accessed through the IRIS DMC. AI at: https://doi.org/10.7914/SN/AI and XB at: https://doi.org/10.7914/SN/XB_1997. The cross-correlations and the final 3-D Vs model are provided in Data Sets S1 and S2 which are archived at: https://doi.org/10.6084/m9.figshare.16702411.

Acknowledgments
The authors appreciate the efforts of all the BRAVOSEIS team members, including Enrique Carmona, Rafa Abella, Paco Carrión, Feli Agüí, Alfonso Ontiveros, José Luis Granja, Iván Fernández, and Rabea Sondershaus, in collecting the data used in this study. The authors thank the German Instrument Pool for Amphibian Seismology (DEPAS, Schmidt-Aursch & Haberland, 2017) for providing seismic instruments for networks 5M and ZX. The authors thank all participants in the BRAVOSEIS 2018, 2019, and 2020 cruises and all staff involved in the realization of the surveys. We use the Generic Mapping Tools (Wessel et al., 2013) to generate the figures. This research is jointly supported by the BRAVOSEIS project (CTM2016-77315-R), AWI, and GFZ. W. Li is also supported by the National Natural Science Foundation of China (41804056) and the Sino-German (CSC-DAAD) Postdoc Scholarship. Constructive comments from the associate editor and two anonymous reviewers helped improve the manuscript. Open access funding enabled and organized by Projekt DEAL.

References

Almendros, J., Carmona, E., Jiménez, V., Díaz-Moreno, A., & Lorenzo, F. (2018). Volcano-tectonic activity at Deception Island volcano following a seismic swarm in the Bransfield Rift (2014–2015). *Geophysical Research Letters*, *45*, 4788–4798. https://doi.org/10.1029/2018GL077490

Almendros, J., Ibáñez, J. M., Alguacil, G., Pezzo, E. D., & Ortiz, R. (1997). Array tracking of the volcanic tremor source at Deception Island, Antarctica. *Geophysical Research Letters*, *24*(23), 3069–3072. https://doi.org/10.1029/97GL03096

Almendros, J., Wilcock, W., Soule, D., Teixidó, T., Vizcaíno, L., Ardanaz, O., et al. (2020). BRAVOSEIS: Geophysical investigation of rifting and volcanism in the Bransfield strait, Antarctica. *Journal of South American Earth Sciences*, *104*, 102834. https://doi.org/10.1016/j.jsames.2020.102834

Argus, D. F., Gordon, R. G., & DeMets, C. (2011). Geologically current motion of 56 plates relative to the no-net-rotation reference frame. *Geochemistry, Geophysics, Geosystems*, *12*, Q11001. https://doi.org/10.1029/2011GC003751

Barker, D. H. N., & Austin, J. A. (1998). Rift propagation, detachment faulting, and associated magmatism in Bransfield Strait, Antarctic Peninsula. *Journal of Geophysical Research*, *103*(B10), 24017–24043. https://doi.org/10.1029/98JB01117

Barker, D. H. N., Christeson, G. L., Austin, J. A., Jr, & Dalziel, I. W. D. (2003). Backarc basin evolution and cordilleran orogenesis: Insights from new ocean-bottom seismograph refraction profiling in Bransfield Strait, Antarctica. *Geology*, *31*(2), 107–110. https://doi.org/10.1130/0091-7613(2003)031<0107:BBEACO>2.0.CO;2

Bensen, G. D., Ritzwoller, M. H., Barmin, M. P., Levshin, A. L., Lin, F., Moschetti, M. P., et al. (2007). Processing seismic ambient noise data to obtain reliable broad-band surface wave dispersion measurements. *Geophysical Journal International*, *169*(3), 1239–1260. https://doi.org/10.1111/j.1365-246X.2007.03374.x

Berrocoso, M., Fernández-Ros, A., Prates, G., García, A., & Kraus, S. (2016). Geodetic implications on block formation and geodynamic domains in the South Shetland Islands, Antarctic Peninsula. *Tectonophysics*, *666*, 211–219. https://doi.org/10.1016/j.tecto.2015.10.023

Birkenmajer, K. (1994). Evolution of the Pacific margin of the northern Antarctic Peninsula: An overview. *Geologische Rundschau*, *83*(2), 309–321. https://doi.org/10.1007/BF00210547

Biryol, C. B., Lee, S. J., Lees, J. M., & Shore, M. J. (2018). Lithospheric structure of an incipient rift basin: Results from receiver function analysis of Bransfield Strait, NW Antarctic Peninsula. *Polar Science*, *16*, 47–58. https://doi.org/10.1016/j.polar.2018.02.003

Burkett, E. R., & Billen, M. I. (2010). Three-dimensionality of slab detachment due to ridge–trench collision: Laterally simultaneous boudinage versus tear propagation. *Geochemistry, Geophysics, Geosystems*, *11*, Q11012. https://doi.org/10.1029/2010GC003286

Catalán, M., Galindo-Zaldivar, J., Davila, J. M., Martos, Y. M., Maldonado, A., Gambôa, L., & Schreider, A. A. (2013). Initial stages of oceanic spreading in the Bransfield Rift from magnetic and gravity data analysis. *Tectonophysics*, *585*, 102–112. https://doi.org/10.1016/j.tecto.2012.09.016

Christensen, N. I., & Mooney, W. D. (1995). Seismic velocity structure and composition of the continental crust: A global view. *Journal of Geophysical Research*, *100*(B6), 9761–9788. https://doi.org/10.1029/95JB00259

Christeson, G. L., Barker, D. H. N., Austin, J. A., & Dalziel, I. W. D. (2003). Deep crustal structure of Bransfield Strait: Initiation of a back arc basin by rift reactivation and propagation. *Journal of Geophysical Research*, *108*(B10), 2492. https://doi.org/10.1029/2003JB002468

Dziak, R. P., Park, M., Lee, W. S., Matsumoto, H., Bohnenstiehl, D. R., & Haxel, J. H. (2010). Tectonomagmatic activity and ice dynamics in the Bransfield Strait back-arc basin, Antarctica. *Journal of Geophysical Research*, *115*, B01102. https://doi.org/10.1029/2009JB006295

Eagles, G., Gohl, K., & Larter, R. D. (2004). High-resolution animated tectonic reconstruction of the South Pacific and West Antarctic Margin. *Geochemistry, Geophysics, Geosystems*, *5*, Q07002. https://doi.org/10.1029/2003GC000657

Eagles, G., & Jokat, W. (2014). Tectonic reconstructions for paleobathymetry in Drake Passage. *Tectonophysics*, *611*, 28–50. https://doi.org/10.1016/j.tecto.2013.11.021

Eagles, G., & Scott, B. G. C. (2014). Plate convergence west of Patagonia and the Antarctic Peninsula since 61 Ma. *Global and Planetary Change*, *123*, 189–198. https://doi.org/10.1016/j.gloplacha.2014.08.002

Fang, H., Yao, H., Zhang, H., Huang, Y.-C., & van der Hilst, R. D. (2015). Direct inversion of surface wave dispersion for three-dimensional shallow crustal structure based on ray tracing: Methodology and application. *Geophysical Journal International*, *201*(3), 1251–1263. https://doi.org/10.1093/gji/ggv080

Fretzdorff, S., Worthington, T. J., Haase, K. M., Hékinian, R., Franz, L., Keller, R. A., & Stoffers, P. (2004). Magmatism in the Bransfield Basin: Rifting of the South Shetland Arc? *Journal of Geophysical Research*, *109*, B12208. https://doi.org/10.1029/2004JB003046

Galindo-Zaldívar, J., Gamboa, L., Maldonado, A., Nakao, S., & Bochu, Y. (2004). Tectonic development of the Bransfield Basin and its prolongation to the South Scotia Ridge, northern Antarctic Peninsula. *Marine Geology*, *206*(1–4), 267–282. https://doi.org/10.1016/j.margeo.2004.02.007

García, M., Ercilla, G., & Alonso, B. (2009). Morphology and sedimentary systems in the Central Bransfield Basin, Antarctic Peninsula: Sedimentary dynamics from shelf to basin. *Basin Research*, *21*(3), 295–314. https://doi.org/10.1111/j.1365-2117.2008.00386.x

García, M., Ercilla, G., Anderson, J. B., & Alonso, B. (2008). New insights on the post-rift seismic stratigraphic architecture and sedimentary evolution of the Antarctic Peninsula margin (Central Bransfield Basin). *Marine Geology*, *251*(3–4), 167–182. https://doi.org/10.1016/j.margeo.2008.02.006

Geyer, A., Álvarez-Valero, A. M., Gisbert, G., Aulinas, M., Hernández-Barreña, D., Lobo, A., & Marti, J. (2019). Deciphering the evolution of Deception Island's magmatic system. *Scientific Reports*, *9*(1), 373. https://doi.org/10.1038/s41598-018-36188-4

González-Casado, J. M., Robles, J. L. G., & López-Martínez, J. (2000). Bransfield Basin, Antarctic Peninsula: Not a normal backarc basin. *Geology*, *28*(11), 10432–11046. https://doi.org/10.1130/0091-7613(2000)28<1043:BBAPNA>2.0.CO;2

Gràcia, E., Canals, M., Lí Farràn, M., José Prieto, M., Sorribas, J., & Team, G. (1996). Morphostructure and evolution of the central and Eastern Bransfield Basins (NW Antarctic Peninsula). *Marine Geophysical Researches*, *18*(2), 429–448. https://doi.org/10.1007/BF00286088

Haase, K. M., & Beier, C. (2021). Chapter 3.2b Bransfield Strait and James Ross Island: Petrology. *Geological Society, London, Memoirs*, *55*, 285–301. https://doi.org/10.1144/M55-2018-37

Heit, B., Yuan, X., Almendros, J., Abella, R., Carmona, E., Aguí, F., & Carrión, P. (2020). *BRAVOSEIS onshore seismic array*. GFZ Data Services. https://doi.org/10.14470/0Z7563857972

Herrmann, R. B. (2013). Computer Programs in Seismology: An evolving tool for instruction and research. *Seismological Research Letters*, *84*(6), 1081–1088. https://doi.org/10.1785/0220110096

Istituto Nazionale Di Oceanografia E Di Geofisica Sperimentale. (1992). Antarctic seismographic Argentinean Italian network—OGS. International federation of digital seismograph networks [Data set]. https://doi.org/10.7914/SN/AI

Janik, T., Grad, M., Guterch, A., & Środa, P. (2014). The deep seismic structure of the Earth's crust along the Antarctic Peninsula—A summary of the results from Polish geodynamical expeditions. *Global and Planetary Change*, *123*, 213–222. https://doi.org/10.1016/j.gloplacha.2014.08.018

Jiménez Morales, V., Almendros, J., & Carmona, E. (2017). Detection of long-duration tremors at Deception Island volcano, Antarctica. *Journal of Volcanology and Geothermal Research*, *347*, 234–249. https://doi.org/10.1016/j.jvolgeores.2017.09.016

Keller, R. A., Fisk, M. R., Smellie, J. L., Strelin, J. A., & Lawver, L. A. (2002). Geochemistry of back arc basin volcanism in Bransfield Strait, Antarctica: Subducted contributions and along-axis variations. *Journal of Geophysical Research*, *107*(B8), 2171. https://doi.org/10.1029/2001JB000444

Klinkhammer, G. P., Chin, C. S., Keller, R. A., Dählmann, A., Sahling, H., Sarthou, G., et al. (2001). Discovery of new hydrothermal vent sites in Bransfield Strait, Antarctica. *Earth and Planetary Science Letters*, *193*(3–4), 395–407. https://doi.org/10.1016/S0012-821X(01)00536-2

Larter, R. D., & Barker, P. F. (1991). Effects of ridge crest–trench interaction on Antarctic-Phoenix Spreading: Forces on a young subducting plate. *Journal of Geophysical Research*, *96*(B12), 19583–19607. https://doi.org/10.1029/91JB02053

Leat, P. T., & Riley, T. R. (2021). Chapter 3.1a Antarctic Peninsula and South Shetland Islands: volcanology, *Geological Society, London, Memoirs*, *55*, 185–212. https://doi.org/10.1144/M55-2018-52

Livermore, R., Balanyá, J. C., Maldonado, A., Martínez, J. M., Rodríguez-Fernández, J., de Galdeano, C. S., et al. (2000). Autopsy on a dead spreading center: The Phoenix Ridge, Drake Passage, Antarctica. *Geology*, *28*(7), 6072–6610. https://doi.org/10.1130/0091-7613(2000)28<607:AOADSC>2.0.CO;2

Lloyd, A. J., Wiens, D. A., Zhu, H., Tromp, J., Nyblade, A. A., Aster, R. C., et al. (2020). Seismic structure of the Antarctic upper mantle imaged with adjoint tomography. *Journal of Geophysical Research: Solid Earth*, *125*, 1–33. https://doi.org/10.1029/2019JB017823

Lodolo, E., & Pérez, L. F. (2015). An abandoned rift in the southwestern part of the South Scotia Ridge (Antarctica): Implications for the genesis of the Bransfield Strait. *Tectonics*, *34*, 2451–2464. https://doi.org/10.1002/2015TC004041

Mantovani, E., Viti, M., Babbucci, D., Tamburelli, C., & Albarello, D. (2001). Back arc extension: Which driving mechanism? *Journal of the Virtual Explorer*, *3*, 17–44. https://doi.org/10.3809/jvirtex.2001.00025

Martínez-Garzón, P., Kwiatek, G., Ickrath, M., & Bohnhoff, M. (2014). MSATSI: A MATLAB package for stress inversion combining solid classic methodology, a new simplified user-handling, and a visualization tool. *Seismological Research Letters*, *85*(4), 896–904. https://doi.org/10.1785/0220130189

McCabe, R. (1984). Implications of paleomagnetic data on the collision related bending of island arcs. *Tectonics*, *3*(4), 409–428. https://doi.org/10.1029/TC003i004p00409

Molnar, P., & Atwater, T. (1978). Interarc spreading and Cordilleran tectonics as alternates related to the age of subducted oceanic lithosphere. *Earth and Planetary Science Letters*, *41*(3), 330–340. https://doi.org/10.1016/0012-821X(78)90187-5

Moresi, L., Betts, P. G., Miller, M. S., & Cayley, R. A. (2014). Dynamics of continental accretion. *Nature*, *508*(7495), 245–248. https://doi.org/10.1038/nature13033

Parera-Portell, J. A., Mancilla, F. de L., Morales, J., Almendros, J., & Jiménez-Morales, V. (2021). Structure of the crust and upper mantle beneath the Bransfield Strait (Antarctica) using P receiver functions. *Tectonophysics*, *802*, 228744. https://doi.org/10.1016/j.tecto.2021.228744

Park, Y., Kim, K.-H., Lee, J., Yoo, H. J., & Plasencia, L. M. P. (2012). P-wave velocity structure beneath the northern Antarctic Peninsula: Evidence of a steeply subducting slab and a deep-rooted low-velocity anomaly beneath the Central Bransfield Basin. *Geophysical Journal International*, *191*(3). 932–938. https://doi.org/10.1111/j.1365-246X.2012.05684.x

Pedrera, A., Ruiz-Constán, A., Heredia, N., Galindo-Zaldívar, J., Bohoyo, F., Marín-Lechado, C., et al. (2012). The fracture system and the melt emplacement beneath the Deception Island active volcano, South Shetland Islands, Antarctica. *Antarctic Science*, *24*(2), 173–182. https://doi.org/10.1017/S0954102011000794

Pérez-Gussinyé, M. (2013). A tectonic model for hyperextension at magma-poor rifted margins: An example from the West Iberia–Newfoundland conjugate margins. *Geological Society, London, Special Publications*, *369*(1), 403–427. https://doi.org/10.1144/SP369.19

Peron-Pinvidic, G., Manatschal, G., & Osmundsen, P. T. (2013). Structural comparison of archetypal Atlantic rifted margins: A review of observations and concepts. *Marine and Petroleum Geology*, *43*, 21–47. https://doi.org/10.1016/j.marpetgeo.2013.02.002

Petersen, S., Herzig, P. M., Schwarz-Schampera, U., Hannington, M. D., & Jonasson, I. R. (2004). Hydrothermal precipitates associated with bimodal volcanism in the Central Bransfield Strait, Antarctica. *Mineralium Deposita*, *39*(3), 358–379. https://doi.org/10.1007/s00126-004-0414-3

Prieto, M. J., Canals, M., Ercilla, G., & de Batist, M. (1998). Structure and geodynamic evolution of the Central Bransfield Basin (NW Antarctica) from seismic reflection data. *Marine Geology*, *149*(1–4), 17–38. https://doi.org/10.1016/S0025-3227(98)00038-3

Ritzwoller, M. H., & Feng, L. (2019). Overview of pre- and post-processing of ambient noise correlations. In Nakata, N., Gualtieri, L., & Fichtner, A. (Eds.), *Seismic ambient noise* (pp. 144–187). Cambridge University Press.

Robertson Maurice, S. D., Wiens, D. A., Shore, P. J., Vera, E., & Dorman, L. M. (2003). Seismicity and tectonics of the South Shetland Islands and Bransfield Strait from a regional broadband seismograph deployment. *Journal of Geophysical Research*, *108*(B10), 2461. https://doi.org/10.1029/2003JB002416

Rodrigo, C., Blamey, J. M., Huhn, O., & Provost, C. (2018). Is there an active hydrothermal flux from the Orca Seamount in the Bransfield Strait, Antarctica? *Andean Geology*, *45*(3), 344–356. https://doi.org/10.5027/andgeoV45n3-3086

Schmidt-Aursch, M. C., Almendros, J., & Geissler, W. H. (2021). P*roject BRAVOSEIS: DEPAS ocean-bottom seismometer operations in the Bransfield strait in 2019–2020*. PANGAEA. https://doi.org/10.1594/PANGAEA.934130

Schmidt-Aursch, M. C., & Haberland, C. (2017). DEPAS (Deutscher Geräte-Pool für amphibische Seismologie): German instrument pool for amphibian seismology. *Journal of Large-Scale Research Facilities JLSRF*, *3*, A122. https://doi.org/10.17815/jlsrf-3-165

Sdrolias, M., & Müller, R. D. (2006). Controls on back-arc basin formation. *Geochemistry, Geophysics, Geosystems*, *7*, Q04016. https://doi.org/10.1029/2005GC001090

Shapiro, N. M., Campillo, M., Stehly, L., & Ritzwoller, M. H. (2005). High-resolution surface-wave tomography from ambient seismic noise. *Science*, *307*(5715), 1615–1618. https://doi.org/10.1126/science.1108339

Smellie, J. L. (2002). The 1969 subglacial eruption on Deception Island (Antarctica): Events and processes during an eruption beneath a thin glacier and implications for volcanic hazards. *Geological Society, London, Special Publications*, *202*(1), 59–79. https://doi.org/10.1144/GSL.SP.2002.202.01.04

Smellie, J. L. (2021). Chapter 3.2a Bransfield Strait and James Ross Island: Volcanology. *Geological Society, London, Memoirs*, *55*(1), 227–284. https://doi.org/10.1144/M55-2018-58

Stern, R. J. (2002). Subduction zones. *Reviews of Geophysics*, *40*(4), 1012. https://doi.org/10.1029/2001RG000108

Taylor, F. W., Bevis, M. G., Dalziel, I. W. D., Smalley, R., Frohlich, C., Kendrick, E., et al. (2008). Kinematics and segmentation of the South Shetland Islands-Bransfield basin system, northern Antarctic Peninsula. *Geochemistry, Geophysics, Geosystems*, *9*, Q04035. https://doi.org/10.1029/2007GC001873

Uyeda, S., & Kanamori, H. (1979). Back-arc opening and the mode of subduction. *Journal of Geophysical Research*, *84*(B3), 1049–1061. https://doi.org/10.1029/JB084iB03p01049

Vuan, A., Robertson Maurice, S.D., Wiens, D.A., & Panza, G.F. (2005). Crustal and upper mantle S-wave velocity structure beneath the Bransfield Strait (West Antarctica) from regional surface wave tomography. *Tectonophysics*, *397*(3-4), 241–259. https://doi.org/10.1016/j.tecto.2004.12.011

Wallace, L. M., Ellis, S., & Mann, P. (2009). Collisional model for rapid fore-arc block rotations, arc curvature, and episodic back-arc rifting in subduction settings. *Geochemistry, Geophysics, Geosystems*, *10*, Q05001. https://doi.org/10.1029/2008GC002220

Wallace, L. M., McCaffrey, R., Beavan, J., & Ellis, S. (2005). Rapid microplate rotations and backarc rifting at the transition between collision and subduction. *Geology*, *33*(11), 857–860. https://doi.org/10.1130/G21834.1

Wessel, P., Smith, W. H. F., Scharroo, R., Luis, J., & Wobbe, F. (2013). Generic Mapping Tools: Improved version released. *Eos, Transactions American Geophysical Union*, *94*(45), 409–410. https://doi.org/10.1002/2013EO450001

Wever, T. (1989). The Conrad discontinuity and the top of the reflective lower crust—do they coincide? *Tectonophysics*, *157*(1–3), 39–58. https://doi.org/10.1016/0040-1951(89)90339-9

Wiens, D. A. (1997). A broadband study of the tectonics and structure of the Antarctic Peninsula and Scotia Sea Regions. In *International federation of digital seismograph networks*. https://doi.org/10.7914/SN/XB_1997

Wiens, D. A., Shen, W., & Lloyd, A. (2021). The seismic structure of the Antarctic upper mantle. *Geological Society, London, Memoirs*, *56*, pp. –. https://doi.org/10.1144/M56-2020-18

Zandomeneghi, D., Barclay, A., Almendros, J., Godoy, J. M. I., Wilcock, W. S. D., & Ben-Zvi, T. (2009). Crustal structure of Deception Island volcano from *P* wave seismic tomography: Tectonic and volcanic implications. *Journal of Geophysical Research*, *114*, B06310. https://doi.org/10.1029/2008JB006119

References From the Supporting Information

Angelier, J. (1984). Tectonic analysis of fault slip data sets. *Journal of Geophysical Research*, *89*, 5835–5848. https://doi.org/10.1029/JB089iB07p05835

Green, R. G., Sens-Schönfelder, C., Shapiro, N., Koulakov, I., Tilmann, F., Dreiling, J., et al. (2020). Magmatic and sedimentary structure beneath the Klyuchevskoy volcanic group, Kamchatka, from ambient noise tomography. *Journal of Geophysical Research: Solid Earth*, *125*, e2019JB018900. https://doi.org/10.1029/2019JB018900

Huang, S., Yao, H., Lu, Z., Tian, X., Zheng, Y., Wang, R., et al. (2020). High-resolution 3-D shear-wave velocity model of the Tibetan Plateau: Implications for crustal deformation and porphyry Cu deposit formation. *Journal of Geophysical Research: Solid Earth*, *125*, e2019JB019215. https://doi.org/10.1029/2019JB019215

Köhler, A., Weidle, C., & Maupin, V. (2012). On the effect of topography on surface wave propagation in the ambient noise frequency range. *Journal of Seismology*, *16*(2), 221–231. https://doi.org/10.1007/s10950-011-9264-5

Luo, S., Yao, H., Wang, J., Wang, K., & Liu, B. (2021). Direct inversion of surface wave dispersion data with multiple-grid parametrizations and its application to a dense array in Chao Lake, eastern China. *Geophysical Journal International*, *225*(2), 1432–1452. https://doi.org/10.1093/gji/ggab036

Luo, Y., Yang, Y., Xu, Y., Xu, H., Zhao, K., & Wang, K. (2015). On the limitations of interstation distances in ambient noise tomography. *Geophysical Journal International*, *201*(2), 652–661. https://doi.org/10.1093/gji/ggv043

Maestro, A., López-Martínez, J., Galindo-Zaldívar, J., Bohoyo, F., & Mink, S. (2014). Evolution of the stress field in the southern Scotia Arc from the late Mesozoic to the present-day. *Global and Planetary Change*, *123*, 269–297. https://doi.org/10.1016/j.gloplacha.2014.07.023

Michael, A. J. (1987). Use of focal mechanisms to determine stress: A control study. *Journal of Geophysical Research*, *92*(B1), 357–368. https://doi.org/10.1029/JB092iB01p00357

Rawlinson, N., & Sambridge, M. (2005). The fast marching method: An effective tool for tomographic imaging and tracking multiple phases in complex layered media. *Exploration Geophysics*, *36*(4), 341–350. https://doi.org/10.1071/EG05341

Yao, H., van Der Hilst, R. D., & de Hoop, M. V. (2006). Surface-wave array tomography in SE Tibet from ambient seismic noise and two-station analysis—I. Phase velocity maps. *Geophysical Journal International*, *166*(2), 732–744. https://doi.org/10.1111/j.1365-246X.2006.03028.x